ROYAL SOCIETY OF CHEMISTRY

PAPER

Check for updates

Plasmonic Au–TiO₂ nanowire/nanotube heterostructures for multifunctional photocatalysis: dye and pesticide degradation, water splitting, and antibacterial activity

Ngo Ngoc Uyen, [ID] [ab] Nguyen Chi Toan, [ID] [cde] Nguyen Truong, [f] Ly Anh Tu [ID] [a] and Phuoc Huu Le [ID] *[bcd]

Methylene blue (MB) and pesticide residues in wastewater pose serious environmental and health concerns. In this study, TiO₂ nanowires grown on nanotube arrays (TNWs/TNAs) and their Au nanoparticle-decorated counterparts (Au-TNWs/TNAs) were fabricated for multifunctional applications, including photocatalytic degradation, photoelectrochemical (PEC) water splitting, and antibacterial activity. TNWs/TNAs were synthesized *via* anodization, followed by the deposition of ∼19.5 nm Au nanoparticles (6.8–8.7 at%) using Turkevich synthesis and immersion methods. Both films exhibited uniform morphology with anatase-phase TiO₂. Photocatalytic performance was evaluated under UV-vis light (100 mW cm⁻²) by monitoring the degradation kinetics of MB and four common pesticides—dimethoate (DMT), methiocarb (MTC), carbofuran (CBF), and carbaryl (CBR)—using LC-MS/MS. Au-TNWs/TNAs demonstrated significantly enhanced degradation rate constants (k): 10.41×10^{-3} min⁻¹ for MB, and 19.8, 18.8, 83.0, and 8.73×10^{-2} min⁻¹ for DMT, CBF, MTC, and CBR, respectively, representing 1.2–1.46× improvements over pristine TNWs/TNAs. These enhancements are attributed to the localized surface plasmon resonance (LSPR) effect of Au, which improves visible-light absorption and charge separation. For PEC performance, Au-TNWs/TNAs achieved a high and stable photocurrent density of 0.51 mA cm⁻² under UV-vis illumination (100 mW cm⁻²), representing an ∼70% enhancement compared to the pristine TNWs/TNAs. Additionally, the Au-TNWs/TNAs demonstrated strong antibacterial activity, achieving an *E. coli* inhibition rate of 61.6% under dim laboratory light and up to 99.9% under low-intensity UV-vis irradiation (6.3 mW cm⁻²). These findings highlight the potential of plasmon-enhanced Au–TiO₂ nanowire/nanotube heterostructures as versatile nanomaterials for integrated applications in dye and pesticide photodegradation, PEC water splitting and antimicrobial control.

1. Introduction

Methylene blue (MB) is a synthetic dye widely used in the textile industry and is recognized as a significant water pollutant.[1] Its heterocyclic aromatic structure makes MB highly soluble in water and stable at room temperature and under visible light

exposure.[1,2] Uncontrolled discharge of MB into aquatic environments threatens human health, aquatic ecosystems, and ecological balance.[1,2]

The extensive use of pesticides to boost agricultural productivity has contributed to the contamination of water bodies, raising growing environmental and public health concerns.[3,4] Pesticide residues in wastewater are increasingly identified as emerging contaminants, with potential risks to both ecosystems and human health.[3,4] Among them, dimethoate (DMT), a commonly used organophosphate pesticide, is known for its severe environmental impact and toxic effects on the liver, kidneys, pancreas, brain, and the nervous, immune, and reproductive systems in humans and mammals.[5] Similarly, carbofuran (CBF), a highly toxic *N*-methyl carbamate pesticide, is persistent in soil and water, and under acidic conditions.[6] Its strong anticholinesterase activity poses serious threats to mammals, birds, fish, and wildlife, and in humans, it is linked to endocrine disruption, cytotoxicity, and genotoxicity.[6]

ᵃHo Chi Minh City University of Technology-VNUHCM, 268 Ly Thuong Kiet Street, Dien Hong Ward, Ho Chi Minh City, 70000, Vietnam

ᵇDepartment of Mathematics–Physics–Informatics, Faculty of Basic Sciences, Can Tho University of Medicine and Pharmacy, 179 Nguyen Van Cu Street, Can Tho City 94000, Vietnam

ᶜInternational PhD Program in Plasma and Thin Film Technology, Ming Chi University of Technology, New Taipei City 243303, Taiwan

ᵈCenter for Plasma and Thin Film Technologies, Ming Chi University of Technology, New Taipei City 243303, Taiwan. E-mail: phle@mail.mcut.edu.tw

ᵉFaculty of Pharmacy and Nursing, Tay Do University, 68 Tran Chien Street, Can Tho City, Vietnam

ᶠMekonglab Testing Center – NHONHO Technology Company Limited, K2-17 Vo Nguyen Giap Street, Can Tho City 94000, Vietnam

Methiocarb (MTC), another carbamate pesticide often found in aquatic environments, presents high ecological risks due to the toxicity of both the parent compound and its metabolites.[7,8] Carbaryl (CBR), a broad-spectrum carbamate insecticide with a long half-life, also persists in soil and water, affecting the pituitary, adrenal, and thyroid glands in animals and contributing to ecological degradation.[9,10]

To address the environmental and health concerns associated with dye and pesticide contamination in water, various advanced oxidation processes (AOPs) have been developed, including electro-Fenton oxidation,[11] chlorination,[12] ozonation,[8] biodegradation using *Rhodopseudomonas capsulata*,[13] and semiconductor-based nanophotocatalysis.[14–18] Among these, TiO$_2$-based nanomaterials have emerged as particularly effective due to their strong redox potential, chemical stability, non-toxicity, and cost-effectiveness.[18–21] Regardless of the synthesis method or morphology, nano-TiO$_2$ consistently outperforms photolysis in degrading MB and various pesticides in aqueous environments.[18–22]

The photocatalytic efficiency of TiO$_2$ is governed by several parameters, including surface area, charge transfer efficiency, crystallinity, band gap energy, morphology, agglomeration degree, light absorption, and the presence of defects or dopants.[23–26] To enhance charge transport and reduce recombination, one-dimensional (1D) TiO$_2$ nanostructures – such as nanowires, nanorods, nanobelts, and nanotubes – have been developed.[27–30] In particular, TiO$_2$ nanowires grown on nanotube arrays (TNWs/TNAs) offer a high surface-to-volume ratio and improved axial charge transport, delivering better photocatalytic activity than nanotubes alone.[27–29,31]

However, the wide band gap of TiO$_2$ (~3.2 eV) limits its absorption to the UV range, which constitutes only 3–5% of the solar spectrum.[23–25,27–29,31] To extend its activity into the visible region, noble metal nanoparticles – especially gold (Au) – have been integrated with TiO$_2$ to leverage localized surface plasmon resonance (LSPR) effects.[32–37] The LSPR phenomenon, modulated by nanoparticle size, shape, and the surrounding dielectric environment,[36,38] enhances visible light absorption and facilitates charge separation in metal–semiconductor composites.[33,37,39,40] Compared to quantum dots, which suffer from photodegradation,[41] noble metal nanoparticles offer greater photostability.[33,37,39,40] Au nanoparticles (Au NPs), in particular, are known for their resistance to oxidation, low cytotoxicity, and strong LSPR response.[33,37,39,40] Acting as optical nanoantennas, they sensitize TiO$_2$ to sub-bandgap visible light and promote the formation of additional charge carriers and reactive oxygen species essential for photocatalysis.[33,37,39,40,42]

Several studies have confirmed the improved photocatalytic degradation of organic pollutants by Au-decorated TiO$_2$ under UV-vis illumination, primarily due to LSPR-enhanced charge dynamics.[33,37,39,40,42] While TiO$_2$ nanotube-based architectures have been investigated,[22,32,43] comprehensive studies integrating TNWs/TNAs with Au NPs for simultaneous degradation of multiple pesticide residues are still limited.[44] Therefore, building on the synergistic potential of Au NPs and TNWs/TNAs, this study explores their combined application to enhance photocatalytic degradation of MB and pesticide

mixtures under UV-vis light through the LSPR effect.[33,37,39,40,42] Importantly, the film configuration of Au-decorated TNWs/TNAs not only enhances performance but also enables easy recovery and repeated use without the need for separation, thereby minimizing the risk of secondary pollution from residual catalysts.

Photoelectrochemical (PEC) water splitting has emerged as a highly promising and environmentally friendly strategy for hydrogen production, offering a sustainable alternative to fossil fuels.[45–47] This technique enables the direct conversion of solar energy into chemical energy by splitting water into hydrogen and oxygen in a PEC cell, with no harmful byproducts.[45–47] Typically, PEC devices comprise a semiconducting photo-electrode coupled with a noble metal counter electrode. The development of stable, highly active photoelectrodes is critical to advancing PEC technology toward practical implementation. TiO$_2$-based nanostructures have attracted considerable attention for PEC water splitting due to their excellent chemical and photostability, low cost, and favorable band-edge alignment.[39,48,49] However, pristine TiO$_2$ suffers from a wide bandgap and fast recombination of photogenerated charge carriers,[39,45] leading to limited visible-light absorption and low solar-to-hydrogen efficiency.[48,50] To overcome these limitations, various modification strategies have been developed, including morphological engineering, doping, and noble metal decoration.[39,45,48,49,51,52] Gold, a noble metal with excellent corrosion resistance, exhibits strong LSPR, enabling efficient light harvesting in the visible and infrared regions during photoreactions.[32,39,45] In this work, a modified one-dimensional (1D) nanostructure of TNWs/TNAs is designed to enhance the surface area and directional charge transport, while Au nanoparticle decoration can further improve PEC performance by boosting light absorption and promoting charge separation.[45,53]

In addition to their roles in photocatalysis and PEC water splitting, TiO$_2$ nanostructures also exhibit intrinsic antibacterial properties, particularly under UV light exposure.[46,54,55] Upon irradiation, TiO$_2$ generates reactive oxygen species (ROS), such as hydroxyl radicals and superoxide anions, which can cause severe oxidative damage to bacterial membranes, ultimately leading to cell death.[56–59] *Escherichia coli* (*E. coli*), a widely used model organism in antimicrobial research, poses a robust challenge due to its complex outer membrane and prevalence in contaminated environments. The antimicrobial efficacy of TiO$_2$-based nanomaterials is closely tied to factors such as morphology, particle size, crystal structure, and surface chemistry.[60–62] Notably, the anatase phase of TiO$_2$ demonstrates the highest photocatalytic and antibacterial performance.[63] While the bactericidal effects of TiO$_2$ and Au–TiO$_2$ nanostructures, including nanoparticles and thin films, have been reported,[51,64–66] the antimicrobial behavior of Au-TNWs/TNAs against *E. coli* remains underexplored.

In this work, we demonstrate the superior photocatalytic activity, PEC performance, and antimicrobial efficacy of TNWs/TNAs and Au-decorated TNWs/TNAs in degrading MB and four widely used pesticides—dimethoate, methiocarb, carbofuran, and carbaryl—under UV-vis irradiation. We provide detailed synthesis procedures, structural and morphological

characterization, and mechanistic insights into the observed enhancements. Additionally, a robust and reproducible analytical method based on liquid chromatography-tandem mass spectrometry (LC-MS/MS) is developed to quantitatively monitor the degradation of these pesticide residues in aqueous solutions. This study underscores the multifunctional performance of TNWs/TNAs and Au-TNWs/TNAs for pollutant degradation, PEC water splitting, and antibacterial activity, aiming to reveal the synergistic effects of the modified nanostructuring and plasmonic enhancement.

2. Materials and methods

2.1. Chemicals and reagents

The chemicals employed in this study included ammonium fluoride (NH_4F, 98.99%, SHOWA, Tokyo, Japan), ethylene glycol (99.5%, Merck), chloroauric acid ($HAuCl_4 \cdot 3H_2O$, 99.9%, Merck), sodium borohydride ($NaBH_4$, 99%, Merck), trisodium citrate (Merck), ethanol (70%, JT Baker), acetone (99.5%, JT Baker), and deionized (DI) water produced using a Milli-Q® ultrapure water system. Methylene blue (MB, 99.9%, Merck, India) was selected as a model dye pollutant.

For pesticide degradation studies, four representative standard pesticides were used: dimethoate (98.5% purity, LGC Standards, Germany), methiocarb (99.5% purity, LGC Standards, Germany), carbofuran (99.5% purity, Chem Service Inc., USA), and carbaryl (99.5% purity, Chem Service Inc., USA). Stock solutions of each pesticide were prepared in methanol at a concentration of 1 ppm and stored at 5 °C, remaining stable for up to three weeks. Prior to photocatalytic experiments, these stock solutions were diluted to 200 ppb to simulate environmentally relevant concentrations.

2.2. Preparation of TiO_2 nanowires on nanotube arrays (TNWs/TNAs), Au nanoparticles, and Au-TNWs/TNAs

Titanium dioxide nanowire-on-nanotube arrays (TNWs/TNAs) were fabricated on titanium (Ti) foil (99.0% purity, dimensions: 1.0 × 2.5 cm^2, thickness: 0.4 mm) using a controlled anodization process. Prior to anodic treatment, the Ti substrates underwent sequential ultrasonic cleaning in acetone, methanol, and deionized (DI) water to remove surface contaminants. The cleaned foils were then dried under a stream of nitrogen gas.

The anodization was carried out using an electrolyte composed of 0.5 wt% ammonium fluoride (NH_4F, SHOWA, Tokyo, Japan) dissolved in ethylene glycol with the addition of 3 vol% DI water. A two-electrode setup was employed, where the Ti foil acted as the working electrode (anode) and a stainless-steel plate (SS304) served as the counter electrode (cathode). The anodization process was conducted at a constant voltage of 30 V for 5 hours, resulting in the formation of the TNWs/TNAs architecture (Fig. S1). After anodization, the resulting structures were subjected to thermal treatment in air at 400 °C for 2 hours to induce crystallinity.

Gold nanoparticles (Au NPs) were synthesized *via* the well-established Turkevich reduction method.[67,68] In this

procedure, 10 mL of DI water was combined with 100 μL of 25 mM chloroauric acid ($HAuCl_4 \cdot 3H_3O$, Merck) in a conical flask under vigorous stirring. The mixture was brought to a boil for 10 minutes, after which 300 μL of 1% trisodium citrate solution was rapidly introduced while stirring was continued. A swift color shift to light red indicated the successful nucleation and growth of Au NPs. The reaction mixture was stirred for an additional 5 minutes and then left to cool naturally to room temperature.

To fabricate Au-TNWs/TNAs, the annealed TNWs/TNAs were immersed in the as-synthesized Au nanoparticle solution and kept at room temperature for 8 hours to facilitate uniform surface deposition of Au NPs. The samples were then gently annealed at 120 °C for 1 hour to remove residual solvent and improve interfacial contact between the Au NPs and the TiO_2 framework.

2.3. Characterization

The crystallographic structure and phase composition of the synthesized samples were characterized using an X-ray diffraction system (XRD, Rigaku SmartLab) equipped with an XSPA-400 ER detector and Cu Kα radiation ($\lambda = 1.5406$ Å), operated in $\theta-2\theta$ scan mode. The mean crystallite size was estimated using the Scherrer formula. Surface morphology and film thickness were analyzed using a scanning electron microscope (SEM, JEOL JSM-IT700HR, Japan). Elemental distribution and composition were assessed *via* energy-dispersive X-ray spectroscopy (EDS) using an Oxford probe integrated into the SEM system.

For high-resolution structural analysis at the nanoscale, high-resolution transmission electron microscopy (HRTEM, JEM-2100, JEOL Ltd, Japan) was employed at an accelerating voltage of 200 kV. TEM specimens were prepared by gently scraping the film surface to detach particles, which were subsequently transferred onto copper grids by direct collection of the particles in close proximity.

The elemental composition and chemical states in the optimized Au-decorated TiO_2 film were analyzed using an X-ray photoelectron spectroscopy system (XPS, Thermo Scientific ESCALAB 250Xi), equipped with a monochromated Al Kα X-ray source (photon energy: 1486.6 eV; maximum power: 300 W). Spectral calibration was performed using the C 1s peak at 284.6 eV. Peak deconvolution and quantitative analysis were carried out using XPSPEAK 4.1 software, applying Shirley background correction and Gaussian–Lorentzian mixed fitting functions to ensure high-precision results.

The optical properties and bandgap energies of the TiO_2 nanostructured films were characterized using diffuse reflectance spectroscopy (DRS), conducted with a JASCO V-670 UV-vis-NIR spectrophotometer. Measurements were recorded over the wavelength range of 200–900 nm at a scan speed of 100 nm min^{-1}, with $BaSO_4$ as the reflectance standard.

To investigate the generation of reactive oxygen species (ROS), particularly hydroxyl radicals ($^{\bullet}OH$), electron paramagnetic resonance (EPR) spectroscopy was conducted using a Bruker ELEXSYS-II E580 FT/CW system. The measurements

were performed in the X-band range (9.49–9.88 GHz) with a microwave power of 8.02 mW. For radical trapping, a 50 mM 5-dimethyl-1-pyrroline N-oxide (DMPO) solution was mixed with a small amount of Au–TiO$_2$ powder, obtained by gently scraping the surface of Au-TNWs/TNAs films and transferring the collected material into a vial containing 2-mL deionized water. EPR spectra were recorded under both dark conditions and photo-irradiation, the latter induced using a 500 W xenon arc lamp to simulate UV-vis light exposure.

2.4. Photocatalytic performance evaluation of the TNWs/TNAs and Au-TNWs/TNAs nanostructured films

The photocatalytic efficiencies of both TNWs/TNAs and Au-TNWs/TNAs were assessed by monitoring the degradation of methylene blue (MB) and a mixed solution of four selected pesticides including dimethoate, methiocarb, carbofuran, and carbaryl under UV-vis irradiation (100 mW cm^{-2}) provided by a xenon arc lamp. Prior to illumination, the samples were immersed in 30 mL of either MB solution (initial concentration $C_0 = 10$ mg L^{-1}) or the pesticide mixture (200 ppb) and kept in the dark for 20 minutes to establish adsorption–desorption equilibrium. Photocatalytic reactions were conducted at room temperature (∼30 °C).

For MB degradation studies, aliquots were collected at pre-determined intervals (0, 20, 40, 60, 80, 100, and 120 minutes) and analyzed using a UV-vis spectrophotometer (Hitachi U-2900, Hitachi, Tokyo, Japan) over a wavelength range of 400–800 nm. In the case of pesticide degradation, 1 mL of the reaction solution was withdrawn at 0, 5, 10, 15, 20, and 25 minutes, passed through a 0.22 μm membrane filter, and transferred into dark vials to prevent photodegradation. These samples were then analyzed by liquid chromatography-tandem mass spectrometry (LC-MS/MS; Acquity H-Class, Waters, Milford, MA, USA). A comprehensive description of the LC-MS/MS instrumentation and analytical conditions is provided in SI S2.

2.5. Photoelectrochemical (PEC) water splitting experiments

Photoelectrochemical (PEC) measurements were performed in a standard three-electrode configuration using an Ag/AgCl reference electrode, a Pt counter electrode, and 0.5 M Na$_2$SO$_4$ aqueous electrolyte (pH = 6.8). The working electrodes consisted of TNWs/TNAs and Au-TNWs/TNAs films (effective area: 2.0 cm^2) synthesized on conductive titanium substrates. An SP-200 potentiostat (BioLogic) was used to record current–voltage (I–V) curves under both dark and illuminated conditions at a scan rate of 10 mV s^{-1}. UV-vis irradiation was provided by a 350 W xenon lamp, delivering a light intensity of 100 mW cm^{-2} over the electrode area. Amperometric photoresponse measurements were conducted under chopped illumination (30 s light/dark cycles) at a constant potential of 0.9 V vs. Ag/AgCl to assess photocurrent reversibility. Photocurrent stability was evaluated by monitoring the current density at 0.9 V vs. Ag/AgCl under continuous UV-vis exposure for 1 hour. Electrochemical impedance spectroscopy (EIS) was carried out in the dark and under UV-vis illumination at open-circuit

potential using a 5 mV AC perturbation over the frequency range of 0.03 Hz to 100 kHz.

2.6. Antimicrobial activity tests

The antibacterial activity was evaluated using *Escherichia coli* (ATCC 25922) as the model organism. Bacterial cultures were grown in nutrient broth at 37 °C for 22 hours to reach a concentration of approximately 1×10^8 CFU mL^{-1}. Cell growth was monitored by measuring the optical density at 600 nm (OD$_{600}$), with an OD value of approximately 0.6 indicating logarithmic-phase growth. The culture was subsequently diluted in Luria Bertani (LB) broth (BioShop Canada Inc.) to a working concentration of 1×10^4 CFU mL^{-1}.

For the assay, 100 μL of the diluted bacterial suspension was carefully pipetted onto a 1.0 cm × 2.0 cm area on each test sample (TNWs/TNAs and Au-TNWs/TNAs), which had been pre-sterilized and placed in individual Petri dishes. The samples were then either kept in the dim laboratory light (DLL) or irradiated under weak UV-vis light (253 nm, 32 W, 6.3 mW cm^{-2}) for 10 minutes. Following treatment, the samples were gently rinsed to recover the bacteria and incubated at 37 °C for 22 hours.

Post-incubation, bacterial viability was assessed by counting colony-forming units (CFU mL^{-1}), allowing for quantitative comparison of surviving bacteria under dark and UV-exposed conditions. A schematic representation of the synthesis, characterization, and experimental methodology is shown in Fig. S1 in the SI.

3. Results and discussion

3.1. Crystal structure, morphology, and composition analysis of TiO$_2$ and Au–TiO$_2$ nanostructured films

Fig. 1 displays the X-ray diffraction (XRD) profiles of TNWs/TNAs and Au-TNWs/TNAs. All samples exhibit distinct peaks corresponding to the anatase phase of TiO$_2$, with major reflections observed at 25.1° (101), 37.8° (004), and 53.8° (105), aligning well with the standard JCPDS No. 21-1272 and AMCSD
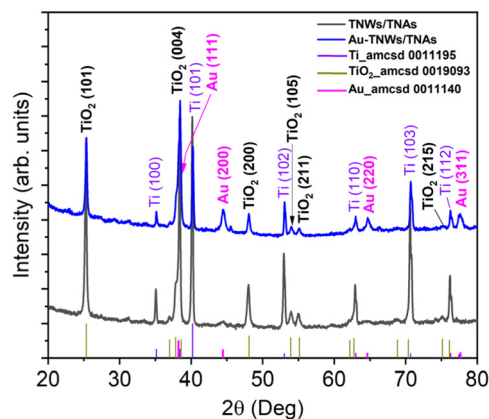
Fig. 1 XRD patterns of TNWs/TNAs and Au-decorated TNWs/TNAs. Reference powder XRD patterns from the AMCSD database for Ti, anatase-phase TiO$_2$, and Au are included in the figure for comparison.

0019093 and previous literature.[29,69,70] The lack of detectable rutile-phase peaks confirms that the synthesized TiO$_2$ nanostructures consist solely of the anatase phase. The diffraction peaks at 44.4°, 64.6°, and 77.6° can be indexed to the (200), (220), and (311) planes of face-centered cubic Au (AMCSD 0011140), respectively. The characteristic Au (111) peak at 38.2° is likely overlapped with the TiO$_2$ (004) reflection. Notably, these XRD results are consistent with those reported for TiO$_2$/Au/TiO$_2$ heterostructures,[46] confirming the successful decoration of anatase TiO$_2$ with nanocrystalline Au nanoparticles. The crystallite sizes of TNWs/TNAs and Au-TNWs/TNAs were estimated to be 28.2 nm and 30.2 nm, respectively, based on peak broadening of the TiO$_2$ (101) reflection using the Scherrer equation: $D = 0.9\lambda/(\beta \cos\theta)$, where $\lambda = 1.5406$ Å is the X-ray wavelength for Cu Kα radiation, and β and θ are the full width at half maximum (FWHM) and the Bragg angle, respectively. These results suggest that the TiO$_2$ samples prepared using different baths exhibit comparable grain sizes. The differences in grain size and crystallinity between TNWs/TNAs and Au-TNWs/TNAs are negligible.

Fig. 2 shows top-view and cross-sectional SEM images of TNWs/TNAs and Au-TNWs/TNAs captured at both low and high magnifications. The TNWs/TNAs display well-defined nanowires, approximately 6.0 μm in length, that are slightly vertically oriented and uniformly distributed over the underlying nanotube arrays. These nanotubes exhibit an average diameter of ∼80 nm and a length of 6.05–6.28 μm (Fig. 2a, b and insets). The Au-TNWs/TNAs exhibit a similar overall morphology, with Au nanoparticles (∼20 nm in diameter) uniformly and homogeneously deposited across the surface of the nanowires and nanotubes, as illustrated in Fig. 2b.

Fig. 3 displays the representative EDS spectrum of Au-TNWs/TNAs, confirming the presence of Au, Ti, and O as the primary elements. The corresponding elemental composition was determined to be 6.77 at% Au, 28.23 at% Ti, and 58.72 at% O. These values suggest that the Ti and O contents are close to the stoichiometric ratio of TiO$_2$. EDS elemental mapping further verified the uniform distribution of Ti, O, and Au across the sample surface. Trace amounts of Na and C were also detected, likely originating from trisodium citrate used during Au NP synthesis. The combined SEM and EDS mapping analyses revealed that Au NPs were relatively homogeneously dispersed over the TNWs/TNAs. This uniform distribution, along with the intimate contact between Au and the TiO$_2$ matrix, is expected to facilitate efficient charge carrier transfer, thereby enhancing the photocatalytic performance.

Fig. 4(a–d) show TEM images captured from various regions of the Au-TNWs/TNAs surface, revealing Au NPs with sizes ranging from 15 to 34 nm (average size of 19.53 ± 4.67 nm, Fig. 4b inset) relatively uniformly dispersed across the TiO$_2$ nanowire–nanotube architecture. Fig. 4c and d highlight a representative region of the Au-TNWs, where the HRTEM image reveals distinct lattice fringes with a d-spacing of 0.23 nm corresponding to the Au (111) planes, and 0.35 nm associated with the TiO$_2$ (101) planes (Fig. 4d). These observations confirm the presence of face-centered cubic (fcc) Au crystallites—consistent with the XRD results shown in Fig. 1—incorporated into anatase TiO$_2$ to form Au–TiO$_2$ heterostructures. In the Turkevich method, auric salt is reduced to aurous salt and elemental Au^0 using trisodium citrate as both a reducing and stabilizing agent.[67,68] The resulting Au^0 atoms serve as nucleation sites for the assembly of aurous species, ultimately forming small Au nanoparticles (NPs).[67,68] Due to gold's high atomic mobility and low crystallization energy barrier, the resulting Au NPs tend to be highly crystalline. This crystallinity is crucial for supporting localized surface plasmon resonance
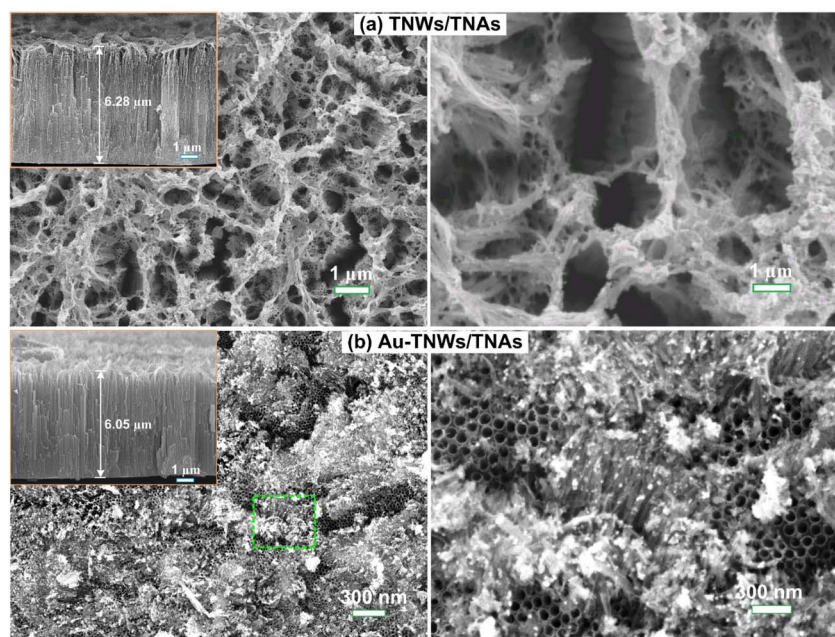

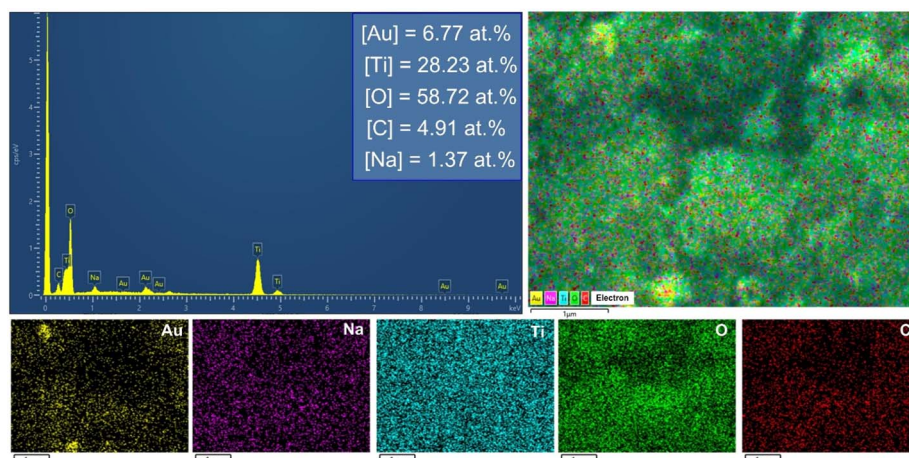Fig. 2 Top-view and cross-sectional SEM images of (a) TNWs/TNAs and (b) Au-TNWs/TNAs.

Fig. 3 EDS spectrum, elemental composition, and elemental mapping of Au-TNWs/TNAs, illustrating the spatial distribution of Au, Ti, and O, along with trace elements Na and C.
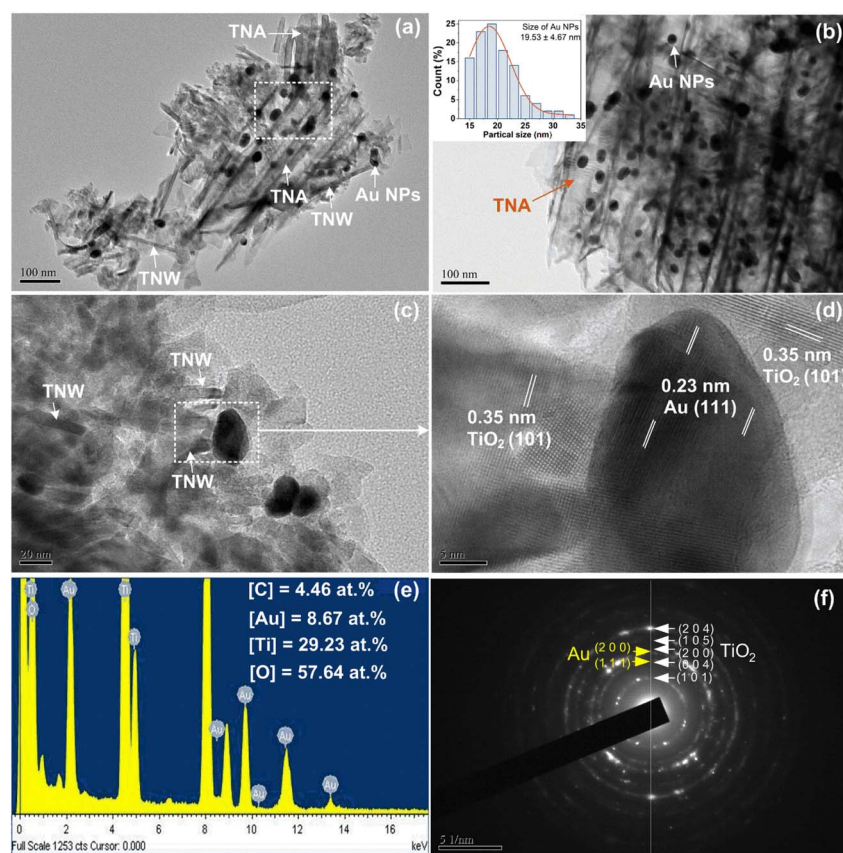

Fig. 4 (a–d) TEM images of Au-TNWs/TNAs captured from various regions of interest. The inset (b) provides the size distribution of the Au NPs. (e) A typical EDS spectrum of Au-TNWs/TNAs, in which presents its elemental atomic % composition. (f) An electron diffraction patterns of Au-TNWs/TNAs.

(LSPR), which plays a key role in enhancing photocatalytic performance through improved light harvesting and hot electron generation.[67,68]

The density of Au NPs varies slightly depending on the location, with Au concentrations ranging from 4.9 to 12.5 at%. Fig. 4e shows a representative EDS spectrum of the Au-TNWs/

TNAs, revealing an elemental composition of 8.67 at% Au, 29.23 at% Ti, 57.64 at% O, and 4.46 at% C. This indicates that the composite retains a nearly stoichiometric TiO_2 composition with notable Au decoration. The presence of carbon is attributed to the adsorption of airborne carbonaceous species. In Fig. 4f, the selected area electron diffraction (SAED) pattern

exhibits spot-ring features, characteristic of nanocrystalline TiO₂ and Au. The *d*-spacing values were calculated using the reciprocal radii of the diffraction rings, and the corresponding lattice planes are annotated in Fig. 4f. In agreement with the XRD results, these findings further validate the presence of Au-decorated TiO₂ nanocrystals.

Fig. 5a presents the wide-scan XPS survey spectra (0–1200 eV) of TNWs/TNAs and Au-TNWs/TNAs. The spectra clearly display the characteristic photoelectron and Auger peaks of Ti and O for TNWs/TNAs, and Ti, O, and Au for Au-TNWs/TNAs, confirming successful surface modification. Additionally, a prominent C 1s peak at 284.6 eV is observed in both samples, attributed to C–C/C–H bonding. This peak arises from ubiquitous adventitious carbon contamination adsorbed on the sample surface due to exposure to ambient air during storage and handling – commonly used for internal calibration in XPS analysis.[33] As shown in Fig. 5b, the Au 4f₇/₂ peak for Au-TNWs/TNAs appears at 83.0 eV, significantly shifted (~1.0 eV) to a lower binding energy (B.E.) compared to the standard value for metallic Au (84.0 eV).[33] This negative shift suggests electron transfer from TiO₂ to Au, most likely originating from oxygen vacancies in TiO₂, resulting in partial charge transfer and the formation of an interfacial dipole. Such a shift is indicative of strong metal–support interaction and has been widely reported in Au/TiO₂ systems.[71]

In Fig. 5c, the high-resolution Ti 2p spectra exhibit doublets at 458.5 eV (2p₃/₂) and 464.3 eV (2p₁/₂) for TNWs/TNAs, characteristic of Ti⁴⁺ in TiO₂.[33] In Au-TNWs/TNAs, these peaks shift slightly to 458.7 eV and 464.4 eV, respectively. The observed ~0.2 eV increase in B.E. indicates a reduction in electron density around Ti atoms, corroborating the electron transfer from TiO₂ to Au

NPs.[33,71] This result aligns with previous findings for Au nanocrystal–TiO₂ nanotube arrays.[72] Fig. 5d displays the deconvoluted O 1s spectra, revealing two main components: the low B.E. peak at ~529.7 eV (TNWs/TNAs) and ~529.9 eV (Au-TNWs/TNAs) corresponds to lattice oxygen (O²⁻ in TiO₂), while the higher B.E. peak at ~531.4 eV in both cases is attributed to surface hydroxyl groups (Ti–OH) or chemisorbed species such as carbonyl groups (C=O).[32] Consistent with the Ti 2p trend, a slight upward shift (~0.2 eV) in the O 1s lattice oxygen peak is also evident in Au-TNWs/TNAs, further corroborating the electron depletion in TiO₂ due to interfacial charge redistribution toward Au.[72]

3.2. Photocatalytic activity in degradation of methylene blue by TiO₂ and Au–TiO₂

The photolysis and photocatalytic degradation kinetics of TNWs/TNAs and Au-TNWs/TNAs were analysed using the Langmuir–Hinshelwood model,[73] based on a pseudo-first-order kinetic approximation: $C_t = C_0 \times e^{-kt}$, where C_0 is the initial concentration, C_t is the concentration at time t, and k is the reaction rate constant (min⁻¹). The degradation kinetics of MB and four pesticides were investigated under UV-vis irradiation (100 mW cm⁻²) *via* photolysis and photocatalysis using TNWs/TNAs and Au-TNWs/TNAs. The degradation was monitored by tracking the decrease in the characteristic absorption peak of MB at 659 nm and the reduction in LC-MS/MS peak areas of the pesticides–dimethoate (DMT), carbofuran (CBF), malathion (MTC), and carbaryl (CBR) (Fig. 6a, b, and S2, Table S3).

The reaction rate constants (*k*) in MB degradation under the three conditions are shown in Fig. 6c. Photolysis yields the
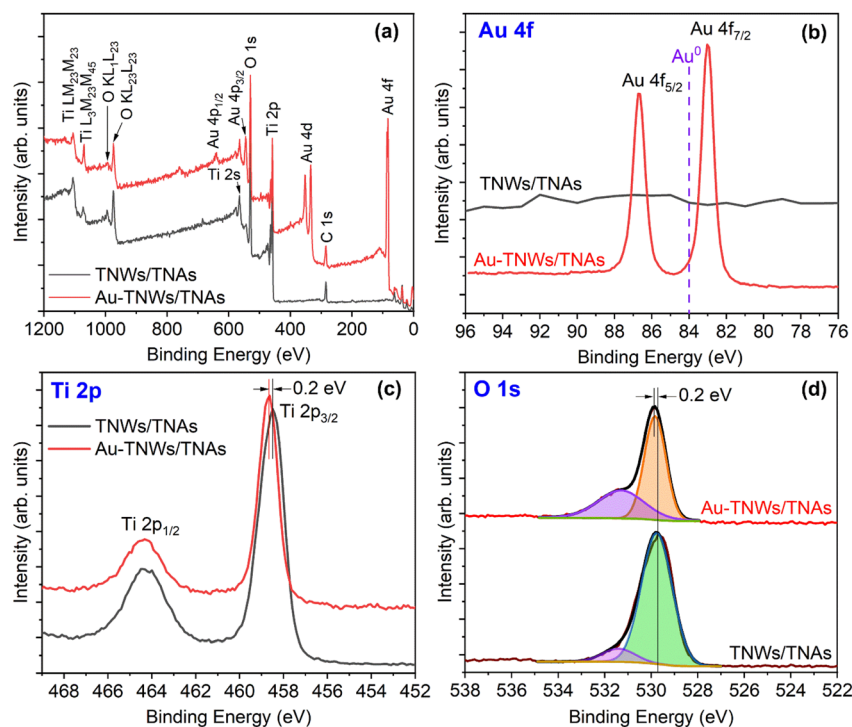

Fig. 5 XPS spectra of TNWs/TNAs and Au-TNWs/TNAs: (a) wide range survey scan (0–1200 eV), (b) Au 4f, (c) Ti 2p, and (d) O 1s high-resolution spectra of TNWs/TNAs and Au-TNWs/TNAs.
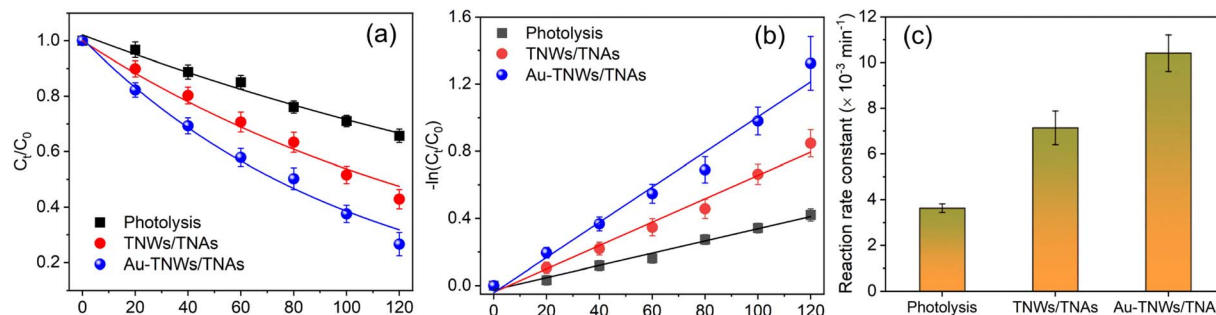
Fig. 6 (a) Photodegradation kinetics of methylene blue (MB) under UV-vis irradiation *via* photolysis and photocatalysis using TNWs/TNAs and Au-TNWs/TNAs. (b) Corresponding $-\ln(C_t/C_0)$ *vs.* time plot derived from the data in (a). (c) Reaction rate constants (k) for MB degradation under photolytic and photocatalytic conditions using TNWs/TNAs and Au-TNWs/TNAs.

lowest k value, 3.63×10^{-3} min^{-1}, indicating that MB remains relatively stable under UV-vis irradiation alone. In contrast, under photocatalytic conditions, the k values increase to 7.14×10^{-3} min^{-1} for TNWs/TNAs and 10.41×10^{-3} min^{-1} for Au-TNWs/TNAs (Fig. 6c). Notably, the presence of Au NPs enhances the photocatalytic efficiency, with the rate constant for Au-TNWs/TNAs approximately -1.4 times higher than that of TNWs/TNAs, underscoring the beneficial role of Au in boosting TiO$_2$ activity.

Compared with previously reported results, the k value of TNWs/TNAs in this study (7.14×10^{-3} min^{-1}) is three time higher than the reported k of 13.05×10^{-2} h^{-1} (or 2.18×10^{-3} min^{-1}) for 40 nm-TNWs/20 nm-TNAs.[28] The observed enhancement is likely due to the greater surface area of TNWs/TNAs in this work, as they feature thicker TNAs and longer TNWs compared to the 40 nm-TNWs/20 nm-TNAs as well as the stronger UV-vis light source than that in ref. 28. In comparison, the k value of Au-TNWs/TNAs 1(0.41 × 10^{-3} min^{-1}) is comparable to that of Ag/TiO$_2$ nanoparticles (0.65 h^{-1} or 10.83×10^{-3} min^{-1}) reported in ref. 74.

To evaluate stability and reusability, Au-TNWs/TNAs underwent four consecutive cycles of MB photocatalytic degradation under identical conditions, as shown in Fig. 7 and S3. Before each cycle, the samples were immersed in deionized water for 2 hours and annealed at 70 °C for 1 hour to remove surface

impurities and improve Au–TiO$_2$ adhesion through thermal treatment. Although the reaction rate constant slightly decreased from 10.41×10^{-3} to 9.40×10^{-3} min^{-1} – a reduction of just 9.7% (Fig. 7b) – the material retained strong photocatalytic performance, achieving approximately 74% MB removal after 120 minutes of irradiation in the fourth cycle (Fig. 7a). The modest drop in activity may be attributed to residual MB or degradation by-products on the surface, as well as minor Au loss during the soaking and drying steps.

3.3. Photodegradation of dimethoate (DMT), carbofuran (CBF), methiocarb (MTC) and carbaryl (CBR) pesticides by TiO$_2$ and Au–TiO$_2$

Building on the strong photocatalytic performance of Au-TNWs/TNAs in MB degradation, this material was further evaluated for pesticide degradation, using TNWs/TNAs as a reference. Fig. 8a presents the degradation of DMT under UV-vis illumination (100 mW cm^{-2}) *via* photolysis and photocatalysis with TNWs/TNAs and Au-TNWs/TNAs. In all cases, the relative concentration of DMT decreased over time (Fig. 8a), following first-order kinetics.

As shown in Fig. 8b, the k for photolysis was the lowest across all pesticides, while Au-TNWs/TNAs consistently exhibited the highest photocatalytic activity. For instance, in the degradation
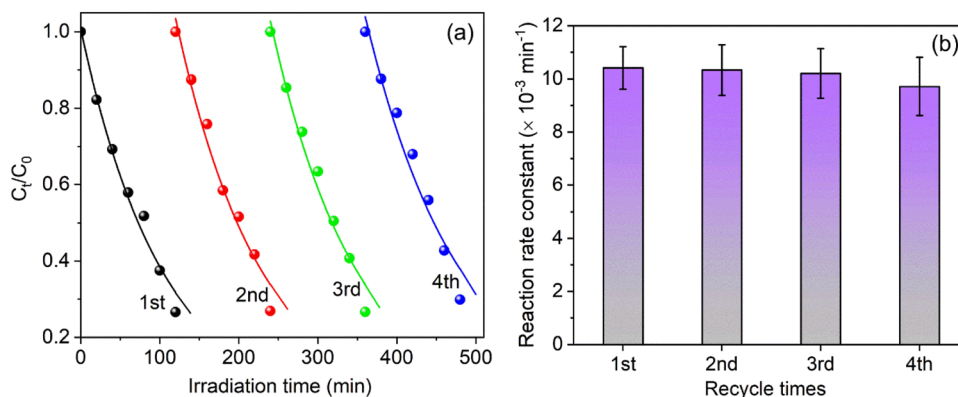

Fig. 7 (a) Photocatalytic degradation of MB by Au-TNWs/TNAs over four consecutive cycles. (b) Corresponding reaction rate constants (k) as a function of cycle number.
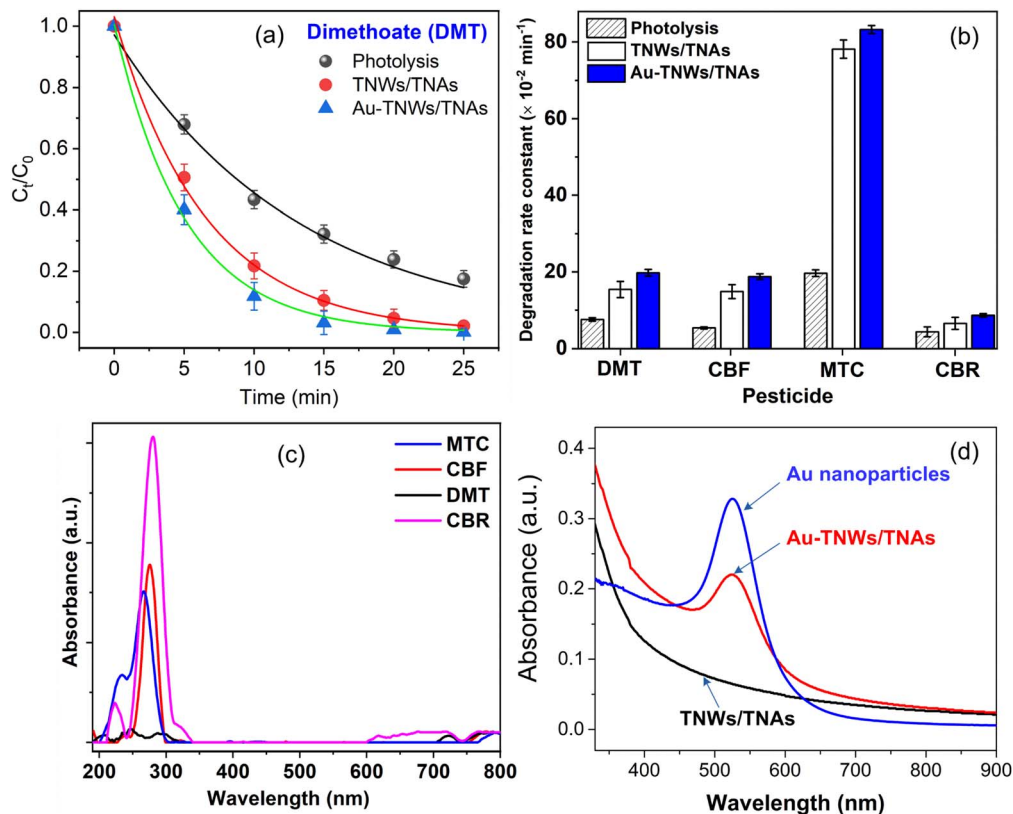
Fig. 8 (a) Photodegradation kinetics of dimethoate (DMT) under UV-vis irradiation (96 mW cm^{-2}) *via* photolysis and photocatalysis using TNWs/TNAs and Au-TNWs/TNAs. (b) Reaction rate constants (k) for the degradation of four pesticides—DMT, methiocarb (MTC), carbofuran (CBF), and carbaryl (CBR)—under photolytic and photocatalytic conditions (initial concentration: 200 ppb). (c) Optical absorption spectra of Au NPs, TNWs/TNAs, and Au-TNWs/TNAs. (d) UV-vis absorption spectra of DMT, MTC, CBF, and CBR (200–800 nm).

of DMT, the k values were 7.5×10^{-2} min^{-1} for photolysis, 15.4×10^{-2} min^{-1} for TNWs/TNAs, and 19.8×10^{-2} min^{-1} for Au-TNWs/TNAs. A similar trend was observed for CBF, with corresponding k values of 5.3×10^{-2} min^{-1}, 14.9×10^{-2} min^{-1}, and 18.8×10^{-2} min^{-1}. For MTC, the k values were significantly higher – 19.7×10^{-2} min^{-1}, 78.0×10^{-2} min^{-1}, and 83.0×10^{-2} min^{-1} – highlighting its rapid degradation. In the case of CBR, the k values were 4.3×10^{-2} min^{-1}, 6.51×10^{-2} min^{-1}, and 8.73×10^{-2} min^{-1} under photolysis, TNWs/TNAs, and Au-TNWs/TNAs, respectively. Generally, the incorporation of Au NPs into TNWs/TNAs improved the reaction rate constant by approximately 1.2 times compared to TNWs/TNAs alone, and by about 2.6 times compared to photolysis, demonstrating the enhanced photocatalytic performance of the hybrid material. Supporting results from Table S3 and Fig. S3 further confirm this trend, showing a consistent decline in LC-MS/MS peak areas for DMT, CBF, MTC, and CBR during photocatalytic treatment using Au-TNWs/TNAs.

Among the four studied pesticides, methiocarb (MTC) exhibited the fastest degradation under UV-vis irradiation (Fig. 8b), while dimethoate (DMT), carbofuran (CBF), and carbaryl (CBR) showed comparatively slower degradation rates. These variations can be primarily attributed to differences in their molecular structures, functional groups, and optical absorption properties.[75,76] MTC contains a phenyl ring,

a carbamate group, and a thiomethyl moiety. The presence of the aromatic ring facilitates π–π* transitions, resulting in strong UV-vis absorption,[77,78] as confirmed in Fig. 8c. This efficient light absorption, combined with the reactive sulfur-containing group, makes MTC particularly susceptible to photodegradation, especially in the presence of Au-modified TiO$_2$, which promotes charge separation and reactive oxygen species (ROS) generation.[78,79] Although CBF and CBR also exhibit strong UV absorption (Fig. 8c), their degradation proceeds more slowly due to their greater structural stability. CBR contains two aromatic rings and a carbamate group, which not only enhance conjugation but also increase molecular rigidity and resistance to photocatalytic attack.[80–82] CBF features a fused benzofuran ring and an amide group, both of which contribute to electron delocalization and chemical stability.[82] The amide linkage in CBF is more stable than the carbamate group in CBR, contributing further to its reduced photocatalytic reactivity.[81]

DMT has the simplest structure among the four pesticides, lacking any aromatic ring. Instead, it contains a thioether, phosphorodiamidate, and ester functionalities. Its weak UV-vis absorbance limits photon capture and results in a low photocatalytic performance.[16,83] Furthermore, the electron-donating alkyl groups and the absence of conjugated π-systems reduce its susceptibility to ROS attack during photocatalysis.[16] Briefly, these structural and electronic factors explain why MTC

degrades more rapidly than CBF, CBR, and DMT, under identical TNWs/TNAs and Au-TNWs/TNAs photocatalytic conditions.

Since the materials were in film form, the TNWs/TNAs and Au-TNWs/TNAs films were ultrasonicated in a DI water container. The resulting suspensions were diluted, and their absorption spectra were measured using a UV-vis spectrophotometer. As shown in Fig. 8d, TNWs/TNAs displayed strong absorption in the UV region below 387 nm. In contrast, Au NPs exhibited a distinct absorption peak at 536 nm due to the localized surface plasmon resonance (LSPR) characteristic of Au NPs.[40] Because the synthesized Au NPs had a non-uniform size distribution (average diameter: 19.5 ± 4.7 nm), the Au-TNWs/TNAs composite demonstrated a broadened absorption band in the visible range (450–620 nm). This broadening is a result of LSPR effects, which are highly dependent on nanoparticle size, shape, and distribution.[84] The extended visible-light absorption contributed by Au NPs enhances light harvesting and facilitates charge separation at the Au–TiO$_2$ interface, ultimately improving photocatalytic efficiency (Fig. 8d).

The diffuse reflectance spectra (DRS), shown in the inset of Fig. 9, were used to estimate the optical band gaps of the TNWs/TNAs and Au-TNWs/TNAs films. The band gap values were determined by extrapolating the linear portion of the $[F(R_\infty) \cdot h\nu]^{0.5}$ plots, based on an indirect electronic transition. The estimated band gaps were 3.13 eV for TNWs/TNAs and 3.01 eV for Au-TNWs/TNAs (Fig. 9). The slight reduction in the band gap observed for the Au-decorated TiO$_2$ may be attributed to the formation of Schottky junctions at the Au/TiO$_2$ interface, which alters the local electronic environment and enables sub-bandgap optical transitions or red-shifted absorption features. Notably, more significant band gap narrowing ($E_g = 2.6$–2.8 eV) in Au–TiO$_2$ systems has been reported in previous studies.[53] Meanwhile, the band gap of the pristine TNWs/TNAs closely matches the well-established range for anatase TiO$_2$, typically between 3.10 and 3.22 eV.[85–88] It is also worth mentioning that no LSPR peak was observed in the DRS spectrum of Au-TNWs/TNAs, likely due to the low reflectance intensity (below 25%). The absence of a distinct LSPR feature in this case is consistent with earlier reports on similar Au/TiO$_2$ nanocomposite systems.[33,53]

Fig. 10a illustrates a proposed mechanism for the enhanced photocatalytic activity of Au NP-decorated TiO$_2$. During photocatalysis, nano-TiO$_2$ is photoexcited by UV light, which promotes electrons from the valence band (VB) to the conduction band (CB), leaving behind positive holes in the VB. Simultaneously, under visible light irradiation, Au NPs are excited due to their LSPR, generating energetic plasmon-induced electron–hole pairs. Plasmonic electrons from Au can be injected into the CB of TiO$_2$, while photogenerated electrons from the TiO$_2$ CB can transfer to Au and recombine with plasmon-induced holes (Fig. 10a).[89] Electrons originating from both TiO$_2$ and Au can react with dissolved O$_2$ in the solution, producing superoxide radicals (O$_2^{\bullet-}$), while the remaining holes oxidize water to generate hydroxyl radicals ($^\bullet$OH). These reactive oxygen species (e.g., $^\bullet$OH and O$_2^{\bullet-}$) effectively degrade the organic MB pollutant and pesticides through stepwise oxidation, ultimately producing small molecules like SO$_4^{2-}$, PO$_4^{3-}$, NH$_4^+$, NO$_3^-$, NO$_2^-$, CO$_2$, and H$_2$O.[16,76] The enhanced photocatalytic activity of Au-TNWs/TNAs over pristine TNWs/TNAs arises from the LSPR of Au nanoparticles, which extends light absorption into the visible range and facilitates charge separation by acting as electron sinks, thereby reducing recombination and increasing reactive radical formation.

The EPR spectrum in Fig. 10b confirms the photoinduced generation of $^\bullet$OH using DMPO as a spin trap under UV-vis irradiation. No signal is observed in the dark, indicating that $^\bullet$OH formation is light-dependent. Upon the UV-vis illumination, the signal intensity increases progressively from 0 to 6 minutes, reflecting the accumulation of $^\bullet$OH radicals during photocatalysis. While the typical quartet signal of the DMPO–$^\bullet$OH adduct ($1:2:2:1$ ratio) is expected, additional peaks are observed. These deviations likely result from overlapping signals of other radical adducts such as DMPO–$^\bullet$OOH, instability and secondary reactions of DMPO–$^\bullet$OH, and possible interactions with the Au–TiO$_2$ surface that alter the magnetic environment or stabilize surface-bound radicals. Collectively, these factors contribute to the broader and more complex EPR spectra compared to that of pure DMPO–$^\bullet$OH.

In this study, Au-TNWs/TNAs demonstrated superior photocatalytic performance, achieving 99.87% DMT degradation within 25 minutes, compared to 95.2% for TNWs/TNAs under identical conditions. This efficiency far surpasses that of the TiO$_2$ P25/polymer film system, which required 3 hours for complete DMT degradation.[90] For CBR removal, Au-TNWs/TNAs and TNWs/TNAs achieved 92.4% and 88.18% degradation, respectively, with corresponding reaction rate constants of 8.73×10^{-2} and 6.51×10^{-2} min^{-1} – both significantly higher than the 2.2–2.5×10^{-2} min^{-1} reported by Jampawal et al.[91] using TiO$_2$-coated glass fiber filters under sunlight. These findings
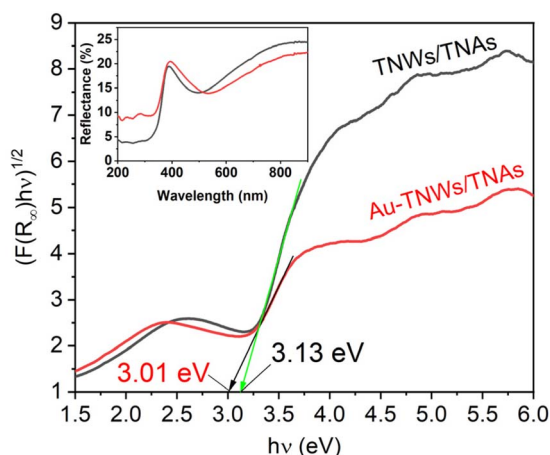
Fig. 9 Tauc plots derived from the transformed Kubelka–Munk function $[F(R_\infty) \cdot h\nu]^{0.5}$ as a function of photon energy, used to estimate the optical band gaps of TNWs/TNAs and Au-TNWs/TNAs. The extrapolated linear regions indicate the corresponding band gap energies. The inset shows the diffuse reflectance spectra (DRS) of both samples.
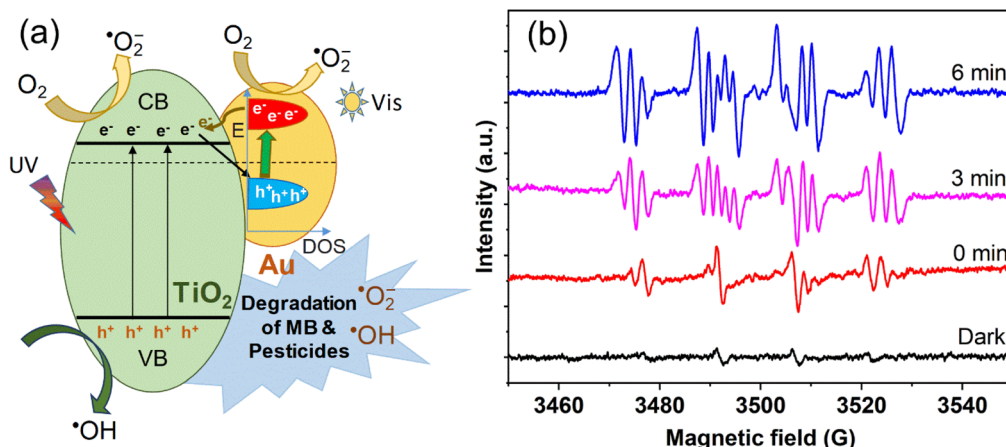
Fig. 10 (a) Proposed mechanism for the photocatalytic degradation of methylene blue (MB) and pesticides by Au–TiO$_2$ under UV-vis illumination. (b) DMPO–$^{\bullet}$OH radical EPR spectrum for Au-TNWs/TNAs.

highlight the enhanced activity of Au-TNWs/TNAs. It is worth noting that direct comparison of photocatalytic performance across different studies remains challenging due to substantial variations in material characteristics (*e.g.*, morphology, crystallinity, surface area, elemental composition, decoration density, and doping) and experimental parameters (*e.g.*, catalyst dosage, light intensity, pollutant type, and concentration). Nonetheless, TiO$_2$-based nanomaterials in this work showed consistent and effective reductions in MB and pesticides under UV-visible light.

3.4. Photoelectrochemical (PEC) water splitting and antibacterial performance of TiO$_2$ and Au–TiO$_2$

Fig. 11a presents the linear sweep voltammetry (LSV) profiles of both TNWs/TNAs and Au-TNWs/TNAs photoanodes, recorded over a potential range of 0 to 1.6 V *versus* Ag/AgCl. In the absence of light, both electrodes exhibited negligible background current, indicating minimal electrochemical activity under dark conditions. Upon UV-vis irradiation, the TNWs/TNAs generated a stable photocurrent density of approximately 0.30 mA cm^{-2} across the 0.4–1.6 V range (Fig. 11a). Notably, the photocurrent density of Au-TNWs/TNAs reached a high value of ~0.51 mA cm^{-2} at 0.9 V *vs.* Ag/AgCl, significantly outperforming the pristine TNWs/TNAs. This 70%-enhancement clearly reflects the positive role of plasmonic Au NPs in boosting the PEC performance by improving light absorption and promoting more efficient charge generation, separation, and transport in the Au–TiO$_2$ heterostructure.

To evaluate the photoconversion efficiency (η), the measured potential (*vs.* Ag/AgCl) was first converted to the reversible hydrogen electrode (RHE) scale using the Nernst equation:[48]

$$E_{\mathrm{RHE}} = E_{\mathrm{Ag/AgCl}} + 0.059 \times \mathrm{pH} + E^0_{\mathrm{Ag/AgCl}}$$

Given that the pH of the Na$_2$SO$_4$ electrolyte was 6.9 and $E^0_{\mathrm{Ag/AgCl}} = 0.194$ V at 25 °C, the potential conversion becomes:

$$E_{\mathrm{RHE}} = E_{\mathrm{Ag/AgCl}} + 0.601 \text{ (volt)}$$

The photoconversion efficiency was calculated using the following expression:[48]

$$\eta = I(E_{\mathrm{rev}}^{\theta} - V)/J_{\mathrm{light}}$$

where I is the measured photocurrent density (mA cm^{-2}), $E_{\mathrm{rev}}^{\theta}$ is the standard water-splitting potential (1.23 V *vs.* RHE), V is the applied potential (*vs.* RHE), and J_{light} is the incident light intensity (0.1 W cm^{-2}).

As shown in Fig. 11b, the η of the pristine TNWs/TNAs reached a maximum of 0.86% at 0.81 V *vs.* RHE, whereas Au-TNWs/TNAs showed a slightly higher efficiency of 0.95% at 0.83 V *vs.* RHE. This improvement is attributed to the LSPR effect of the Au nanocrystals, which enhances light absorption and charge generation. Comparatively, the obtained efficiency for Au-TNWs/TNAs surpasses the reported η of 0.75% at 0.6 V *vs.* RHE for B–TiO$_2$/Au NPs/Au NRs;[48] however, it remains slightly lower than the 1.25% reported for Au/TiO$_2$ branched nanorod arrays (BNRs).[45]

The transient photocurrent response (*I–t* curves) measured at 0.9 V *vs.* Ag/AgCl under chopped UV-vis illumination is presented in Fig. 11c. Both photoanodes displayed rapid and reproducible photocurrent responses upon light on/off switching, indicating prompt charge separation and transport within the TiO$_2$ and Au–TiO$_2$ heterojunctions. Au-TNWs/TNAs achieved a maximum photocurrent density of 0.51 mA cm^{-2}—representing a 1.72-fold increase compared to the unmodified TNWs/TNAs. This value exceeds the photocurrent of Au/TiO$_2$ BNRs (0.13 mA cm^{-2})[45] but remains lower than those of B–TiO$_2$/Au NPs (1.3 mA cm^{-2}) and B–TiO$_2$/Au NPs/Au NRs (1.5 mA cm^{-2}).[48] Such variations are likely influenced by differences in TiO$_2$ morphology, Au nanoparticle size, shape, and loading.

Fig. 11d evaluates the long-term photoelectrochemical stability of the electrodes under continuous UV-vis irradiation for 1 hour. Both TNWs/TNAs and Au-TNWs/TNAs maintained relatively stable photocurrents—approximately 0.30 mA cm^{-2}
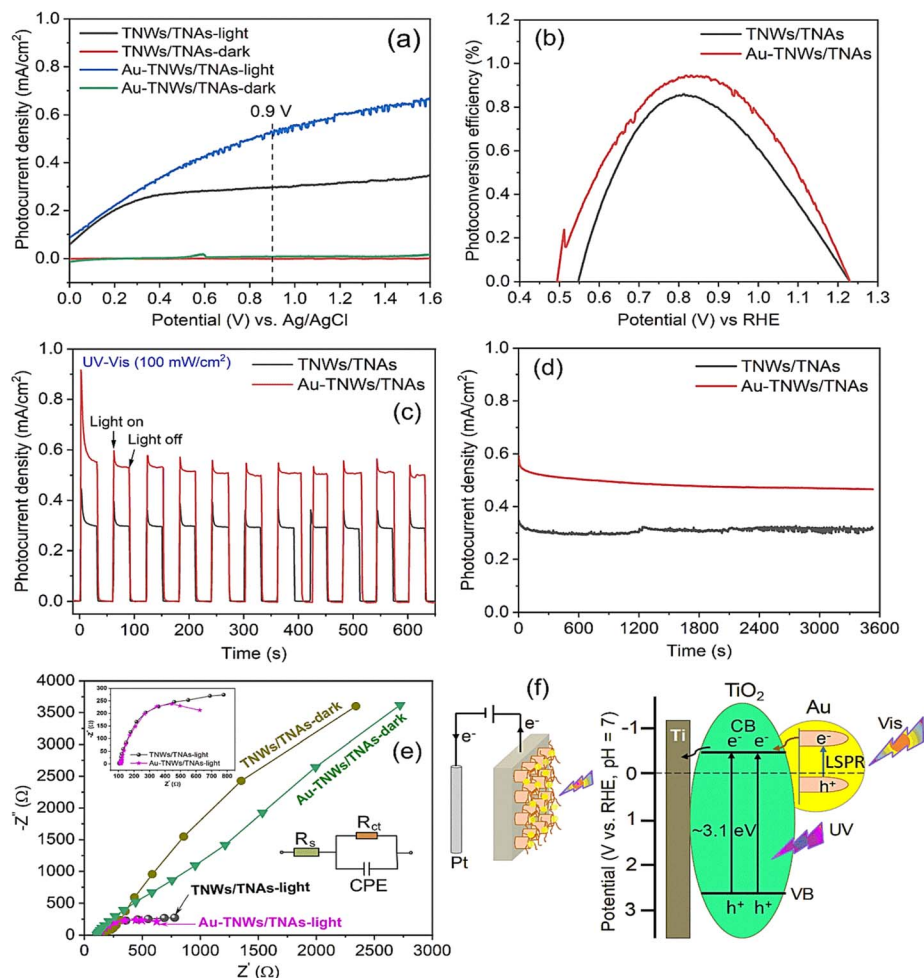
Fig. 11 (a and b) Linear sweep voltammetry (LSV) curves and calculated photoconversion efficiency (%) of TNWs/TNAs and Au-TNWs/TNAs measured under dark and UV-visible illumination (100 mW cm^{-2}) conditions. (c) Amperometric I–t responses recorded at 0.9 V $vs.$ Ag/AgCl (approximately 1.5 V $vs.$ RHE) under chopped UV-vis light irradiation. (d) Photocurrent stability of TNWs/TNAs and Au-TNWs/TNAs photo-electrodes measured at 0.9 V $vs.$ Ag/AgCl under continuous UV-visible illumination. (e) Electrochemical impedance spectroscopy (EIS) Nyquist plots of the photoelectrodes measured under dark and UV-vis illumination conditions. (f) Simplified schematic illustration, energy level diagram, and charge transfer mechanism in Au–TiO$_2$ under UV-visible illumination.

and 0.48 mA cm^{-2}, respectively—with minimal decay over time. These results suggest that the structural and functional integrity of both materials is preserved during extended PEC operation, consistent with observations in Au/TiO$_2$ BNRs.[45]

To further probe the interfacial charge dynamics, electrochemical impedance spectroscopy (EIS) was conducted under dark and illuminated conditions, with the resulting Nyquist plots shown in Fig. 11e. The semicircular arc in the high-frequency region of the Nyquist plot reflects the charge-transfer resistance at the electrode–electrolyte interface. The EIS data were fitted using an equivalent circuit model (R_s + R_{ct}/CPE), where R_s represents the series resistance, R_{ct} denotes the charge transfer resistance, and CPE is the constant phase element representing double-layer capacitance.

The extracted R_{ct} values were 5486 Ω for TNWs/TNAs in the dark and 2646 Ω for Au-TNWs/TNAs in the dark, which decreased significantly to 561 Ω and 461 Ω, respectively, under UV-vis illumination. These results clearly demonstrate that Au decoration substantially reduces the interfacial resistance in

both dark and light environments. The lower R_{ct} observed under illumination is attributed to the enhanced generation and separation of electron–hole pairs, which accelerate interfacial charge transfer. In contrast, the higher R_{ct} in the dark is a consequence of the reduced availability of charge carriers. Overall, the incorporation of plasmonic Au NPs not only improves light harvesting via LSPR but also facilitates faster and more efficient electron transport, leading to enhanced PEC water-splitting performance.

Based on the above findings, the proposed charge transfer mechanism in the Au–TiO$_2$ heterostructure is illustrated in Fig. 11f. Under UV-vis illumination, TiO$_2$ absorbs photons, promoting electrons from the VB to the CB of the TNWs/TNAs, thereby generating electron–hole pairs. Simultaneously, the plasmonic Au NPs absorb vis light through the LSPR effect, producing energetic "hot" electrons and holes. Although a Schottky barrier is typically formed at the Au–TiO$_2$ interface, which can act as an electron trap, the LSPR-induced hot electrons possess sufficient energy to overcome this barrier and are
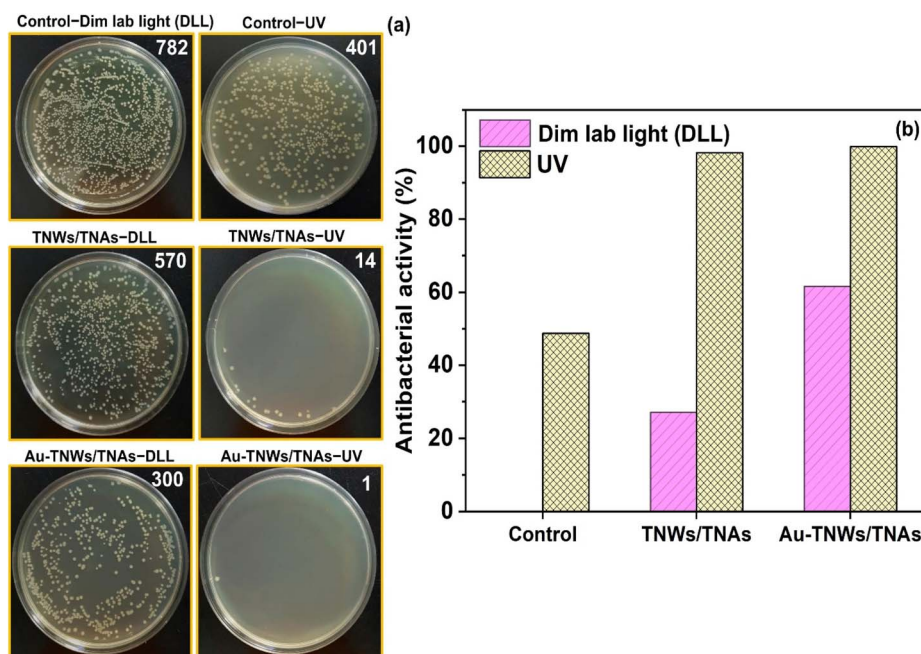
Fig. 12 (a) Photographs of *E. coli* colonies after 22 hours of incubation under different conditions: control, TNWs/TNAs, and Au-TNWs/TNAs, evaluated both in dim laboratory light (DLL) and after 10 minutes of UV irradiation (6.3 mW cm^{-2}); colony counts for each condition are indicated in the top-right corner of the corresponding images. (b) Quantitative comparison of antibacterial activity (%) for each sample under the respective conditions.

injected into the CB of TiO$_2$. Under an applied bias during the PEC process, these photogenerated electrons are efficiently transported through the TiO$_2$ network to the underlying titanium substrate and then to the counter electrode,[48] where they participate in the water reduction reaction. Meanwhile, the remaining holes in TiO$_2$ and Au contribute to the oxidation half-reaction, completing the water splitting process.

Fig. 12 shows the antibacterial performance of TNWs/TNAs and Au-TNWs/TNAs under dim laboratory light (DLL) and weak UV irradiation (253 nm, 32 W, 6.3 mW cm^{-2}), with bacterial colony counts noted in the upper right corner of each sample. Under UV exposure, TNWs/TNAs achieved a high antibacterial efficiency of 98.2%, while Au-TNWs/TNAs reached an even higher rate of 99.9%. In contrast, UV irradiation alone exhibited only 48.7% inhibition of *E. coli*, clearly highlighting the critical role of the photocatalysts. This antibacterial activity is attributed to the generation of reactive oxygen species (ROS) such as hydroxyl radicals (·OH) and superoxide anions (O$_2$·$^-$) by TiO$_2$, which are well known for disrupting bacterial membranes and intracellular structures.[51,92] These ROS rapidly damage the bacterial cell wall and membrane, penetrate the cytoplasm, and interfere with essential biological functions including respiration, DNA replication, and the uptake of iron and phosphate—cumulatively enhancing antibacterial efficacy.[54] The superior performance of Au-TNWs/TNAs under UV light is attributed to the LSPR effect of Au NPs, which facilitates enhanced electron–hole (e–h) pair generation and separation, thereby increasing ROS production.

Notably, under DLL conditions, TNWs/TNAs still show moderate antibacterial activity (~27.1%), which improves markedly to 61.6% with Au-TNWs/TNAs—surpassing the 48.7%

efficacy achieved under UV light alone (Fig. 12). This DLL-condition activity of TiO$_2$ arises from its ability to disrupt bacterial membranes *via* electrostatic interactions or direct contact with the nanomaterial.[92] Additionally, TiO$_2$ inhibits bacterial aggregation and biofilm formation, both key pathogenic traits.[93]

The significantly improved antibacterial effect of Au-TNWs/TNAs under DLL conditions could be due to the LSPR of Au NPs, which enables the excitation of hot electrons even under low-vis light conditions (DLL). These hot electrons can transfer to TiO$_2$'s conduction band, migrate to the surface, and drive redox reactions, thereby promoting ROS generation. Importantly, the observed *E. coli* inhibition of 99.9% under weak UV and 61.6% under DLL for Au-TNWs/TNAs is comparable to that reported for 1% Au/TiO$_2$, which exhibited a low *E. coli* survival percentage of 32.4% (or 67.6% bacterial killing) under intense 400–700 nm-visible light from a 300 W xenon lamp equipped with filters. Importantly, the Au-TNWs/TNAs achieved a remarkable 99.9% *E. coli* inhibition under weak UV light and 61.6% under dim laboratory light (DLL), which is comparable to the performance of 1% Au/TiO$_2$ that exhibited only 32.4% *E. coli* survival (*i.e.*, 67.6% bacterial inactivation) under strong visible light (400–700 nm) from a 300 W xenon lamp equipped with optical filters.[51]

4. Conclusions

TiO$_2$ nanowires/nanotubes (TNWs/TNAs) were fabricated *via* anodization, and ~19.5 nm Au nanoparticles (6.8–8.7 at%) were synthesized using the Turkevich method and uniformly deposited onto the TNWs/TNAs through an immersion process

to form Au-TNW/TNA heterostructures. Structural and spectroscopic analyses confirmed anatase-phase TiO_2 with uniform Au distribution, intimate metal–semiconductor contact, and efficient interfacial electron transfer. Under UV-vis irradiation, Au-TNWs/TNAs exhibited markedly improved photocatalytic degradation of methylene blue (MB) and four pesticides—dimethoate (DMT), carbofuran (CBF), methiocarb (MTC), and carbaryl (CBR)—compared to pristine TNWs/TNAs. The degradation rate constant for MB increased 1.46-fold (from 7.14×10^{-3} to 10.41×10^{-3} min^{-1}), while pesticide degradation rates rose by $\sim1.2\times$. These enhancements are attributed to the localized surface plasmon resonance (LSPR) effect of Au, which extends light absorption into the visible range, accelerates charge separation, and boosts reactive oxygen species (ROS) generation. The photocatalysts retained $\sim90\%$ of their initial activity after four cycles, indicating excellent stability and reusability. Diffuse reflectance spectroscopy revealed a slight band gap narrowing from 3.13 eV (TNWs/TNAs) to 3.01 eV (Au-TNWs/TNAs), consistent with Schottky junction formation at the Au/TiO_2 interface. Photoelectrochemical tests showed a stable photocurrent density of 0.51 mA cm^{-2} at 0.9 V $vs.$ Ag/AgCl – 70% higher than that of pristine films – and a photoconversion efficiency increase from 0.86% to 0.95%. Electrochemical impedance spectroscopy further confirmed reduced charge-transfer resistance in Au-TNWs/TNAs under illumination, indicating more efficient interfacial electron transport. Antibacterial assays demonstrated 99.9% $E.\ coli$ inactivation under weak UV-vis light (6.3 mW cm^{-2}) and 61.6% under dim laboratory light, both outperforming pristine TNWs/TNAs. This superior antibacterial performance is linked to LSPR-driven hot electron transfer, which enhances ROS-mediated bacterial damage. Overall, Au-TNWs/TNAs integrate high photocatalytic activity, enhanced PEC water-splitting performance, and strong antibacterial capability, making them versatile and recyclable nanomaterials for sustainable water purification, renewable energy production, and microbial control.

Author contributions

Ngo Ngoc Uyen: methodology, investigation, formal analysis, writing original draft preparation. Nguyen Chi Toan, Nguyen Truong: methodology, investigation, formal analysis. Ly Anh Tu: methodology, validation, writing – review and editing, and supervision. Phuoc Huu Le: conceptualization, methodology, formal analysis, resources, validation, writing – review and editing, supervision.

Conflicts of interest

There are no conflicts to declare.

Data availability

The data supporting this article have been included as part of the supplementary information (SI). Supplementary information: synthesis schematics, methods, LC-MS/MS conditions, MB photodegradation by TNWs/TNAs and Au-TNWs/TNAs, and MRM chromatograms of MTC, CBF, CBR, and DMT. See DOI: https://doi.org/10.1039/d5na00765h.

References

1 R. Al-Tohamy, S. S. Ali, F. Li, K. M. Okasha, Y. A. G. Mahmoud, T. Elsamahy, H. Jiao, Y. Fu and J. Sun, *Ecotoxicol. Environ. Saf.*, 2022, **231**, 113160.

2 M. I. Din, R. Khalid, J. Najeeb and Z. Hussain, *J. Cleaner Prod.*, 2021, **298**, 126567.

3 G. Braun, M. Braun, J. Kruse, W. Amelung, F. G. Renaud, C. M. Khoi, M. V. Duong and Z. Sebesvari, *Environ. Int.*, 2019, **127**, 442–451.

4 A. Sharma, V. Kumar, B. Shahzad, M. Tanveer, G. P. S. Sidhu, N. Handa, S. K. Kohli, P. Yadav, A. S. Bali, R. D. Parihar, O. I. Dar, K. Singh, S. Jasrotia, P. Bakshi, M. Ramakrishnan, S. Kumar, R. Bhardwaj and A. K. Thukral, *SN Appl. Sci.*, 2019, **1**, 1446.

5 A. Eken, in *Toxicology*, ed. V. B. Patel and V. R. Preedy, Academic Press, 2021, pp. 59–68, DOI: 10.1016/B978-0-12-819092-0.00007-8.

6 S. Mishra, W. Zhang, Z. Lin, S. Pang, Y. Huang, P. Bhatt and S. Chen, *Chemosphere*, 2020, **259**, 127419.

7 J. Campo, A. Masia, C. Blasco and Y. Pico, *J. Hazard. Mater.*, 2013, **263P**, 146–157.

8 A. Cruz-Alcalde, C. Sans and S. Esplugas, *Chemosphere*, 2017, **186**, 725–732.

9 X. Fadic, F. Placencia, A. M. Dominguez and F. Cereceda-Balic, *Sci. Total Environ.*, 2017, **575**, 146–151.

10 V. C. Moser, P. M. Phillips and K. L. McDaniel, *Toxicology*, 2015, **331**, 1–13.

11 H. Rashid Ahmed and K. F. Kayani, *Inorg. Chem. Commun.*, 2024, **170**, 113467.

12 F. Tian, Z. Qiang, W. Liu and W. Ling, *Chem. Eng. J.*, 2013, **232**, 10–16.

13 P. Wu, L. Xie, W. Mo, B. Wang, H. Ge, X. Sun, Y. Tian, R. Zhao, F. Zhu, Y. Zhang and Y. Wang, *J. Environ. Manage.*, 2019, **249**, 109226.

14 C. B. D. Marien, T. Cottineau, D. Robert and P. Drogui, *Appl. Catal., B*, 2016, **194**, 1–6.

15 J.-Q. Chen, D. Wang, M.-X. Zhu and C.-J. Gao, *Desalination*, 2007, **207**, 87–94.

16 D. Vaya and P. K. Surolia, *Environ. Technol. Innovation*, 2020, **20**, 101128.

17 A. Rafiq, M. Ikram, S. Ali, F. Niaz, M. Khan, Q. Khan and M. Maqbool, *J. Ind. Eng. Chem.*, 2021, **97**, 111–128.

18 N. N. Uyen, L. A. Tu and P. H. Le, *Appl. Phys. A:Mater. Sci. Process.*, 2025, **131**, 302.

19 K. G. Thakre, D. P. Barai and B. A. Bhanvase, *Water Environ. Res.*, 2021, **93**, 2414–2460.

20 N. Thakur, N. Thakur, A. Kumar, V. K. Thakur, S. Kalia, V. Arya, A. Kumar, S. Kumar and G. Z. Kyzas, *Sci. Total Environ.*, 2024, **914**, 169815.

21 S. Sayegh, F. Tanos, A. Nada, G. Lesage, F. Zaviska, E. Petit, V. Rouessac, I. Iatsunskyi, E. Coy, R. Viter, D. Damberga, M. Weber, A. Razzouk, J. Stephan and M. Bechelany, *Dalton Trans.*, 2022, **51**, 2674–2695.

22 T. P. Huynh, T. C. M. V. Do and P. H. Le, *ACS Appl. Nano Mater.*, 2024, **7**, 20012–20023.

23 Q. Xu, L. Zhang, J. Yu, S. Wageh, A. A. Al-Ghamdi and M. Jaroniec, *Mater. Today*, 2018, **21**, 1042–1063.

24 Q. Xu, L. Zhang, B. Cheng, J. Fan and J. Yu, *Chem*, 2020, **6**, 1543–1559.

25 I. Ahmad, Y. Zou, J. Yan, Y. Liu, S. Shukrullah, M. Y. Naz, H. Hussain, W. Q. Khan and N. R. Khalid, *Adv. Colloid Interface Sci.*, 2023, **311**, 102830.

26 S. G. Kumar and L. G. Devi, *J. Phys. Chem. A*, 2011, **115**, 13211–13241.

27 J. Yan and F. Zhou, *J. Mater. Chem.*, 2011, **21**, 9406–9418.

28 M.-Y. Hsu, H.-L. Hsu and J. Leu, *J. Electrochem. Soc.*, 2012, **159**, H722–H727.

29 T. P. Huynh, P. H. Le, L. D. T. Nguyen and T. C. M. V. Do, *Microchem. J.*, 2025, **212**, 113598.

30 X. Wang, Z. Li, J. Shi and Y. Yu, *Chem. Rev.*, 2014, **114**, 9346–9384.

31 J. Tian, Z. Zhao, A. Kumar, R. I. Boughton and H. Liu, *Chem. Soc. Rev.*, 2014, **43**, 6920–6937.

32 N. N. Uyen, L. T. C. Tuyen, L. T. Hieu, T. T. T. Nguyen, H. P. Thao, T. C. M. V. Do, K. T. Nguyen, N. T. N. Hang, S.-R. Jian, L. A. Tu, P. H. Le and C.-W. Luo, *Coatings*, 2022, **12**, 1957.

33 F. Su, T. Wang, R. Lv, J. Zhang, P. Zhang, J. Lu and J. Gong, *Nanoscale*, 2013, **5**, 9001–9009.

34 X. Wei, P. S. Nbelayim, G. Kawamura, H. Muto and A. Matsuda, *Nanotechnology*, 2017, **28**, 135207.

35 Y. Zhuang, L. Liu, X. Wu, Y. Tian, X. Zhou, S. Xu, Z. Xie and Y. Ma, *Part. Part. Syst. Charact.*, 2018, **36**, 1800077.

36 E. Petryayeva and U. J. Krull, *Anal. Chim. Acta*, 2011, **706**, 8–24.

37 T. Bora, D. Zoepfl and J. Dutta, *Sci. Rep.*, 2016, **6**, 26913.

38 C. Li, K. L. Shuford, M. Chen, E. J. Lee and S. O. Cho, *ACS Nano*, 2008, **2**, 1760–1769.

39 Y.-C. Pu, G. Wang, K.-D. Chang, Y. Ling, Y.-K. Lin, B. C. Fitzmorris, C.-M. Liu, X. Lu, Y. Tong, J. Z. Zhang, Y.-J. Hsu and Y. Li, *Nano Lett.*, 2013, **13**, 3817–3823.

40 S. Linic, P. Christopher and D. B. Ingram, *Nat. Mater.*, 2011, **10**, 911–921.

41 F. P. García de Arquer, D. V. Talapin, V. I. Klimov, Y. Arakawa, M. Bayer and E. H. Sargent, *Science*, 373, eaaz8541.

42 M. Alvaro, B. Cojocaru, A. A. Ismail, N. Petrea, B. Ferrer, F. A. Harraz, V. I. Parvulescu and H. Garcia, *Appl. Catal., B*, 2010, **99**, 191–197.

43 K. Lee, A. Mazare and P. Schmuki, *Chem. Rev.*, 2014, **114**, 9385–9454.

44 P. H. Le, T. P. Huynh, T.-P. Chu, L. T. Nguy, N. N. Uyen and T. C. M. V. Do, *Nanoscale Adv.*, 2025, **7**, 3344–3357.

45 F. Su, T. Wang, R. Lv, J. Zhang, P. Zhang, J. Lu and J. Gong, *Nanoscale*, 2013, **5**, 9001–9009.

46 X. Yu, X. Jin, X. Chen, A. Wang, J. Zhang, J. Zhang, Z. Zhao, M. Gao, L. Razzari and H. Liu, *ACS Nano*, 2020, **14**, 13876–13885.

47 S. Bae, T. Moehl, E. Service, M. Kim, P. Adams, Z. Wang, Y. Choi, J. Ryu and S. D. Tilley, *Nat. Commun.*, 2024, **15**, 9439.

48 Z. Cao, Y. Yin, P. Fu, D. Li, Y. Zhou, Z. Wen, Y. Peng, W. Wang, W. Zhou and D. Tang, *J. Electrochem. Soc.*, 2020, **167**, 026509.

49 J.-Y. Choi, Y. Hoon Sung, H.-J. Choi, Y. Doo Kim, D. Huh and H. Lee, *Ceram. Int.*, 2017, **43**, 14063–14067.

50 H. Liu, J. Zhang, Y.-j. Luo, L. Qin, T. Zhang, Y. Xu, X. Li and S.-Z. Kang, *Int. J. Hydrogen Energy*, 2024, **79**, 1–9.

51 J. Zhang, X. Suo, J. Zhang, B. Han, P. Li, Y. Xue and H. Shi, *Mater. Lett.*, 2016, **162**, 235–237.

52 N. Celebi, M. Y. Aydin, F. Soysal, Y. O. Ciftci and K. Salimi, *J. Alloys Compd.*, 2021, **860**, 157908.

53 Y. Yu, W. Wen, X.-Y. Qian, J.-B. Liu and J.-M. Wu, *Sci. Rep.*, 2017, **7**, 41253.

54 D. Carol López de, C. Matias Guerrero, B. M. Fernanda, S. Camilo and G. Maria José, in *Antimicrobial Resistance*, ed. M. Mihai, L. Swee Hua Erin, L. Kok-Song and C. Romeo-Teodor, IntechOpen, Rijeka, 2020, ch. 5, p. 90891, DOI: **10.5772/intechopen.90891**.

55 A. Petica, A. Florea, C. Gaidau, D. Balan and L. Anicai, *J. Mater. Res. Technol.*, 2019, **8**, 41–53.

56 A. Steinbach, D. Svab, L. Korosi, M. Kerenyi, J. Kun, P. Urban, T. Palkovics, T. Kovacs and S. Gyorgy, *Heliyon*, 2024, **10**, e33562.

57 T. Munir, A. Mahmood, N. Abbas, A. Sohail, Y. Khan, S. Rasheed and I. Ali, *ACS Omega*, 2024, **9**, 34841–34847.

58 B. Xue, A. Hou, Y. Du, Y. Qi, H. Jiang, H. Zhou, Z. Zhou and H. Chen, *Surf. Interfaces*, 2023, **39**, 102996.

59 G. Carré, E. Hamon, S. Ennahar, M. Estner, M.-C. Lett, P. Horvatovich, J.-P. Gies, V. Keller, N. Keller and P. Andre, *Appl. Environ. Microbiol.*, 2014, **80**, 2573–2581.

60 C. López de Dicastillo, C. Patiño, M. J. Galotto, J. L. Palma, D. Alburquenque and J. Escrig, *Nanomaterials*, 2018, **8**, 128.

61 R. C. de Oliveira, C. C. de Foggi, M. M. Teixeira, M. D. P. da Silva, M. Assis, E. M. Francisco, B. N. A. d. S. Pimentel, P. F. d. S. Pereira, C. E. Vergani, A. L. Machado, J. Andres, L. Gracia and E. Longo, *ACS Appl. Mater. Interfaces*, 2017, **9**, 11472–11481.

62 Z. He, Q. Cai, H. Fang, G. Situ, J. Qiu, S. Song and J. Chen, *J. Environ. Sci.*, 2013, **25**, 2460–2468.

63 G. Vimbela, S. M. Ngo, C. Fraze, L. Yang and D. A. Stout, *Int. J. Nanomed.*, 2017, **12**, 3941–3965.

64 E. Widyastuti, C.-T. Chiu, J.-L. Hsu and Y. Chieh Lee, *Arabian J. Chem.*, 2023, **16**, 105010.

65 L. S. Daniel, M. T. Joseph, V. Uahengo and M. Hedimbi, *Adv. Mater. Interfaces*, 2024, **11**, 2400035.

66 J. Paniagua-Méndez, S. L. Ramírez-Sandoval, E. Reyes-Uribe and M. E. Contreras-García, *Ceram. Int.*, 2024, **50**, 34421–34430.

67 J. Kimling, M. Maier, B. Okenve, V. Kotaidis, H. Ballot and A. Plech, *J. Phys. Chem. B*, 2006, **110**, 15700–15707.

68 P. Zhao, N. Li and D. Astruc, *Coord. Chem. Rev.*, 2013, **257**, 638–665.

69 L. Sun, J. Cai, Q. Wu, P. Huang, Y. Su and C. Lin, *Electrochim. Acta*, 2013, **108**, 525–531.

70 X. Luan, D. Guan and Y. Wang, *J. Phys. Chem. C*, 2012, **116**, 14257–14263.

71 X. Zheng, X. Yan, J. Ma, X. Yao, J. Zhang and L. Wang, *ACS Appl. Mater. Interfaces*, 2021, **13**, 16498–16506.

72 Z. Zhang, L. Zhang, M. N. Hedhili, H. Zhang and P. Wang, *Nano Lett.*, 2013, **13**, 14–20.

73 C. Dong, M. Zhong, T. Huang, M. Ma, D. Wortmann, M. Brajdic and I. Kelbassa, *ACS Appl. Mater. Interfaces*, 2011, **3**, 4332–4338.

74 H.-C. Tseng and Y.-W. Chen, *Mod. Res. Catal.*, 2020, **09**, 1–19.

75 F. Souiad, A. S. Rodrigues, A. Lopes, L. Ciríaco, M. J. Pacheco, Y. Bendaoud-Boulahlib and A. Fernandes, *Molecules*, 2020, **25**, 5893.

76 H. Yang, S. Zhou, H. Liu, W. Yan, L. Yang and B. Yij, *J. Environ. Sci.*, 2013, **25**, 1680–1686.

77 J. Gao, L. Liu, X. Liu, H. Zhou, J. Lu, S. Huang and Z. Wang, *Bull. Environ. Contam. Toxicol.*, 2009, **82**, 223–229.

78 M. Yeganeh, E. Charkhloo, H. R. Sobhi, A. Esrafili and M. Gholami, *Chem. Eng. J.*, 2022, **428**, 130081.

79 C. M. Hadad, P. R. Rablen and K. B. Wiberg, *J. Org. Chem.*, 1998, **63**, 8668–8681.

80 S. Casado, M. Alonso, B. Herradón, J. V. Tarazona and J. M. A. Navas, *Environ. Toxicol. Chem.*, 2006, **25**, 3141–3147.

81 A. K. Ghosh and M. Brindisi, *J. Med. Chem.*, 2015, **58**, 2895–2940.

82 M. Cui, H. Wang, X. Fan, J. Zhang, C. Xing and W. Yan, *Appl. Surf. Sci.*, 2024, **663**, 160197.

83 Z. Wu, L. Yang, Y. Tang, Z. Qiang and M. Li, *Chemosphere*, 2021, **273**, 129724.

84 V. Amendola, O. M. Bakr and F. Stellacci, *Plasmonics*, 2010, **5**, 85–97.

85 Z. Li, S. Wang, J. Wu and W. Zhou, *Renewable Sustainable Energy Rev.*, 2022, **156**, 111980.

86 P. Makula, M. Pacia and W. Macyk, *J. Phys. Chem. Lett.*, 2018, **9**, 6814–6817.

87 H. Yaghoubi, Z. Li, Y. Chen, H. T. Ngo, V. R. Bhethanabotla, B. Joseph, S. Ma, R. Schlaf and A. Takshi, *ACS Catal.*, 2014, **5**, 327–335.

88 Y. Duan, S. Zhou, Z. Chen, J. Luo, M. Zhang, F. Wang, T. Xu and C. Wang, *Catal. Sci. Technol.*, 2018, **8**, 1395–1403.

89 Y. Zhang, M. Gong, X. Liu, L. Ji, Z. Yang and X. Zhu, *J. Mater. Sci.*, 2019, **54**, 2975–2989.

90 D. N. Priya, J. M. Modak, P. Trebse, R. Zabar and A. M. Raichur, *J. Hazard. Mater.*, 2011, **195**, 214–222.

91 J. Jampawal, S. Supothina and P. Chuaybamroong, *Environ. Sci. Pollut. Res.*, 2022, **29**, 88027–88040.

92 H. H. Bahjat, R. A. Ismail, G. M. Sulaiman and M. S. Jabir, *J. Inorg. Organomet. Polym. Mater.*, 2021, **31**, 3649–3656.

93 A. Kubacka, C. Serrano, M. Ferrer, H. Lünsdorf, P. Bielecki, M. L. Cerrada, M. Fernández-García and M. Fernández-García, *Nano Lett.*, 2007, **7**, 2529–2534.